Author/s:
Ahmed, T;Kuriakose, S;Tawfik, SA;Mayes, ELH;Mazumder, A;Balendhran, S;Spencer, MJS;Akinwande, D;Bhaskaran, M;Sriram, S;Walia, S

Title:
Mixed Ionic-Electronic Charge Transport in Layered Black-Phosphorus for Low-Power Memory

Date:
2021-11-23

Citation:
Ahmed, T., Kuriakose, S., Tawfik, S. A., Mayes, E. L. H., Mazumder, A., Balendhran, S., Spencer, M. J. S., Akinwande, D., Bhaskaran, M., Sriram, S. & Walia, S. (2021). Mixed Ionic-Electronic Charge Transport in Layered Black-Phosphorus for Low-Power Memory. ADVANCED FUNCTIONAL MATERIALS, 32 (10), https://doi.org/10.1002/adfm.202107068.

Mixed ionic-electronic charge transport in layered black-phosphorus for low-power memory

Taimur Ahmed[1,2,], Sruthi Kuriakose,[1,3] Sherif Abdulkader Tawfik[4,5], Edwin L. H. Mayes[6], Aishani Mazumder,[3] Sivacarendran Balendhran[7], Michelle J. S. Spencer[8], Deji Akinwande[9], Madhu Bhaskaran[1], Sharath Sriram[1] and Sumeet Walia[1,3,*]*

[1]Functional Materials and Microsystems Research Group and the Micro Nano Research Facility, RMIT University, Melbourne VIC 3001, Australia

[2]Pak-Austria Fachhochschule: Institute of Applied Sciences and Technology, Haripur, 22620 Pakistan

[3]School of Engineering, RMIT University, Melbourne, VIC 3001, Australia

[4]ARC Centre of Excellence in Exciton Science, School of Science, RMIT University, Melbourne, VIC 3001 Australia

[5]Chemical and Quantum Physics, School of Science, RMIT University, Melbourne VIC 3001, Australia

[6]School of Science, RMIT University, Melbourne, VIC 3001, Australia

[7]School of Physics, The University of Melbourne, VIC 3010, Australia

[8]ARC Centre of Excellence in Future Low-Energy Electronics Technologies, School of Science, RMIT University, Melbourne, VIC 3001, Australia

[9]Microelectronics Research Centre, The University of Texas at Austin, Austin, TX 78758, USA

*Correspondence to: taimur.ahmed@rmit.edu.au, sumeet.walia@rmit.edu.au

Abstract

Availability of computing will be strongly limited by global energy production in 1-2 decades. Computing consumes 4-5% of global electricity supply and continues to increase. This is underpinned by memory and switching devices encountering leakage as they are downscaled. Two-dimensional (2D) materials offer a potential solution to the fundamental problem owing to carrier confinement which significantly reduces scattering events. Here, we use mixed ionic-electronic transport in layered black phosphorus (BP) based vertically

stacked resistance change memories. The memory device relies on a unique interplay between the oxygen and silver ion diffusion through the stack which is generated using a combination of bottom (electrochemically active silver) and top (Indium tin oxide) electrodes. The use of a transparent top-electrode enabled for the first time to conduct spectroscopic characterization of the device and experimentally reveal fundamental mechanisms. Endurance of the devices are observed to be $>10^4$ switching cycles, with ON/OFF current ratio of $>10^7$ and standby power consumption of <5 fW, which effectively suppresses leakage current and sneak paths in a memory array. By undertaking detailed microscopic and spectroscopic investigations, supported by theoretical calculations, this work opens opportunities to enhance resistive switching performances of 2D materials for next-generation information storage and brain-inspired computation.

Keywords

resistive memories, black phosphorus, metal-ion diffusion, layered 2D materials, neuromorphic computation

Introduction

Resistive memory devices have demonstrated significant potential for future high-density data storage mainly owing to their scalability, low power consumption, compatibility with conventional semiconductor technology and ability to implement neuromorphic computing architectures.[1,2] Though continuous intense research in traditional metal-oxide memory devices has achieved these promising results, there remain critical challenges of operational voltages, leakage and sneak path currents.[3] Stochastic nature of charge transport during programming in traditional oxide memory devices (*i.e.*, ionic valence change and movement of metal-cations across the switching layers) could affect stability and reliability of these devices. In this context, vertically stacked van der Waals structure of two-dimensional (2D) materials may offer a significant control in the ionic transport, anisotropic crystallinity and defect incorporation rendering high memory window, low leakage and programming currents.[4-7] Furthermore, recent developments enabling thickness control of 2D materials at the atomic scale pushes the scalability of resistive memory devices down to sub-nanometres and per bit energy consumption to femtojoule.[6,8,9]

Recently, 2D transition-metal dichalcogenides (MX_2, M = Mo, W and X = S, Se, Te),[4,9,10] transition-metal oxide (such as MoO_3),[11] hexagonal boron nitride (*h*-BN)[8,12] and elemental black phosphorus (BP) [13-16] have been used in vertically stacked resistive memory devices to exploit their potential for alternative solutions. For instance, multilevel storage,[17] low energy neuromorphic computation,[5,18] terahertz switching,[19] and scaling down to atomic scale[8,9] are realised in 2D materials based resistive memory devices. Although these results are significant, there are several unaddressed questions regarding the resistive switching endurance and charge transport mechanism in vertically stacked van der

Waals structures. Most of the resistive memory devices based on different 2D materials suffer from low switching endurance (as highlighted in **Table 1**). This can be associated with energy barrier of the van der Waals layers to the out-of-plan nano-ionic (cationic and anionic) charge transport originating from their strain and electronic energies.[20,21] Owing to the high mobility of oxygen ions and low barrier energy for their diffusion, partial oxidation of a 2D material or adding an oxide layer in the vertical stack of switching layers could improve the switching performance of the resistive memory devices.[4,6,7,13,14,16] Furthermore, a range of microscopic and spectroscopic analyses are required to establish a vivid resistive switching mechanism in vertically stacked 2D materials based resistive memory devices.

Unlike 2D transition-metal dichalcogenides and *h*-BN, BP is known to rapidly oxidise upon exposure to ambient and forms a layer of complex phosphorus-oxide (P_xO_y) on its surface which is considered detrimental for electronic devices.[22,23] However, natural oxidation of BP has recently been harnessed to engineer new characteristics for multifunctional electronic and optoelectronic devices.[24-26] As such, this offers an advantage of high oxygen ion mobility across heterogeneously integrated 2D material and its native oxide for high performance resistive memory devices. Herein, we use transparent indium tin oxide (ITO) as an oxide top electrode in our ITO/BP/Ag cross-bar resistive memory devices to locally oxidise BP across the vertical stack by diffusing oxygen ions and metal Ag ions (from bottom Ag electrode) under an applied electric field. Raman mapping technique is used for the first time as a non-destructive approach to pinpoint locally oxidised region in a switching device. This is enabled by a transparent top electrode (ITO). The locally oxidised BP provides a path for coupled ionic-electronic charge transport across the stack and stable resistive switching for $>10^4$ switching cycles (highest than any reported BP based resistive memory devices), a

large memory window of $>10^7$ and a low standby power consumption of <5 fW. Furthermore, our BP resistive memory devices retain their switching characteristics for more than 25 days without the use of any additional surface passivation steps, demonstrating environmental stability.

Results

The vertical BP resistive memory devices are fabricated in cross-point configuration by sandwiching mechanically exfoliated multilayer-BP flakes between bottom Ag and top ITO electrodes. **Figure 1**a shows the Scanning Electron Microscope (SEM) micrograph of a representative vertical BP resistive memory device. The cross-point configuration of BP resistive memory devices ensures that vertical charge transport is confined within the <6 μm^2 device area, without any contributions of lateral transport. The associated Energy Dispersive X-ray Spectroscopy (EDS) elemental maps of the representative BP resistive memory device (Figure 1b-e) show Ag as bottom and ITO as top electrodes. Although single cross-point memory devices are required to explore memory fundamentals, large-scale memory integration, data storage and neuromorphic computation are contingent on the demonstration of memory operations in an array. Recently, memory arrays have be demonstrated on different 2D materials,[21,27-30] including mechanically exfoliated BP.[13] In this work, single cross-point BP memory devices are fabricated on mechanically exfoliated flakes to undertake extensive memory characterizations and underpin the switching mechanism. Figure 1f shows an atomic force microscope (AFM) topographic scan of the transferred multilayer-BP flake on the bottom Ag electrode. An average thickness of ~19.1 nm is measured from the AFM scan (Figure 1g). Several devices in the range of ~8-100 nm thickness are also fabricated (see Section S1, Supporting Information) to characterise

thickness dependent characteristics of our ITO/BP/Ag memory devices. To vividly present underlaying switching mechanisms in our BP resistive memory devices, it is very important to conduct all electrical, optical and spectroscopic characterisations on the same device. As such, mostly data and characterisations presented in the manuscript are collected from the same device with BP flake of thickness ~19.1 nm, shown in Figure 1a. However, the resistive switching characteristics of the devices with different thicknesses are discussed in Supporting Information (see Section S3).

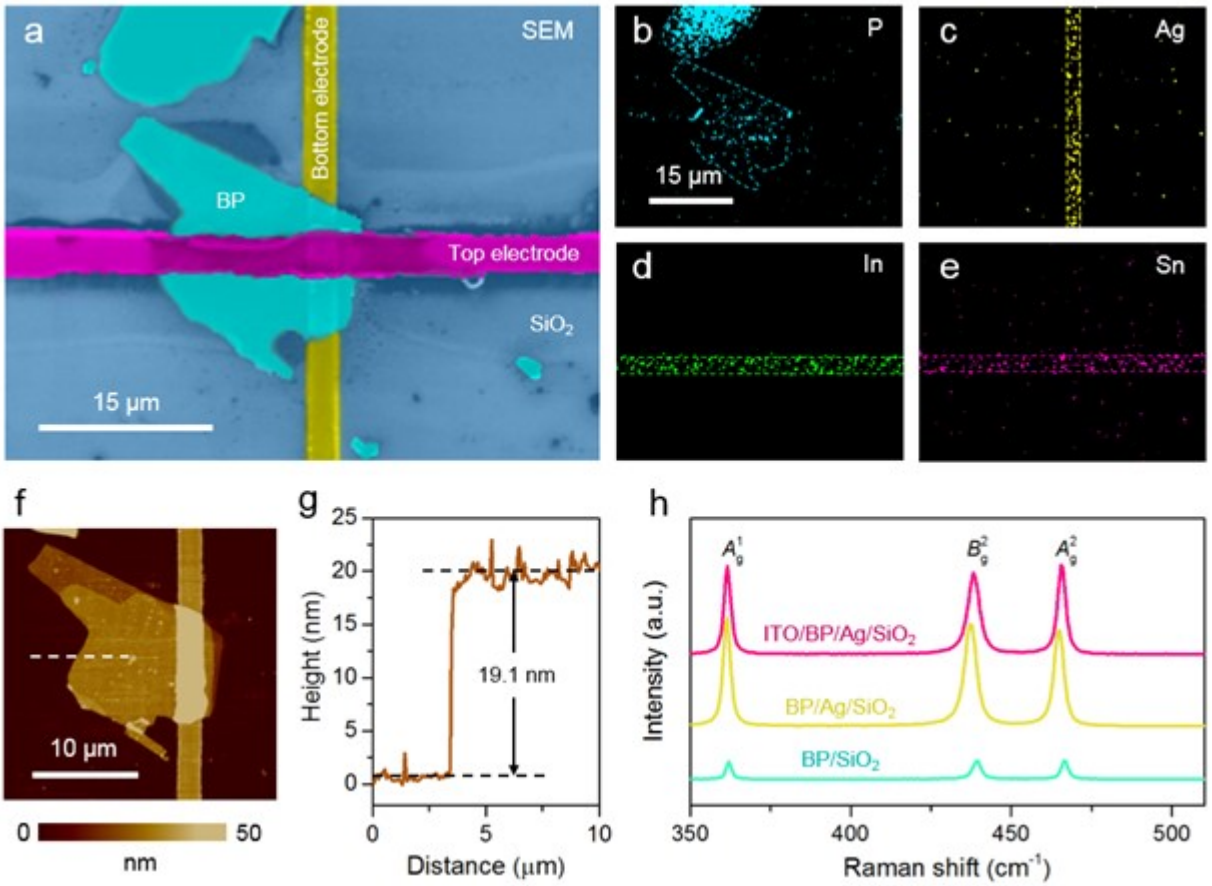

Figure 1. Structure of BP memory devices and spectroscopic characterisation. (a) False-coloured scanning electron microscope (SEM) micrograph of a representative BP resistive memory

cross-point device. Energy dispersive X-ray spectroscopy elemental map of (b) phosphorus (P), (c) silver (Ag), (d) indium (In) and (e) tin (Sn). (f) Atomic force microscope topographic scan of the mechanically exfoliated and transferred BP flake on a bottom Ag electrode. (g) Height profile of the BP flake in (f). (h) Raman spectra collected from bare BP on SiO_2 substrate, BP on bottom Ag electrode and the cross-point ITO/BP/Ag region of pristine BP resistive memory device.

Raman point spectra are collected from different locations of a pristine device including bare BP on SiO_2, BP on bottom Ag electrode and BP sandwiched between top ITO and bottom Ag electrodes, *i.e.*, cross-point region (Figure 1h). Raman spectra show all three signature peaks of BP corresponding to the A^1_g, B^2_g and A^2_g vibrational modes, where A^1_g mode originates primarily from the out-of-plane vibrations of phosphorus atoms along the *c*-axis, while the B^2_g and A^2_g modes arise from the in-plane vibrations of phosphorus atoms along the *armchair* and *zigzag*, respectively. Relatively higher intensities of Raman spectral modes of BP/Ag and ITO/BP/Ag (as compared to BP/SiO_2) can be associated with the enhanced Raman scattering effect of the bottom Ag electrode.[31,32] Interestingly, the high optical transmission (>80%, see Section 2 in Supporting Information) of top ITO electrode in visible wavelengths allows Raman spectroscopy on the cross-point region which is used to analyse oxygen ion migration during resistive switching operation of BP resistive memory devices, as discussed later in the manuscript.

The resistive switching behaviour of BP resistive memory devices is characterised by applying bias to the bottom Ag electrode and grounding the top ITO electrode (**Figure 2**a). As depicted by *I–V* characteristics in Figure 2b, our BP resistive memory devices exhibit bipolar resistive switching where a positive voltage sweep on bottom Ag electrode SET the

high resistive state (HRS) of the device to a low resistive state (LRS) and a negative bias sweep RESET the device from LRS to HRS.

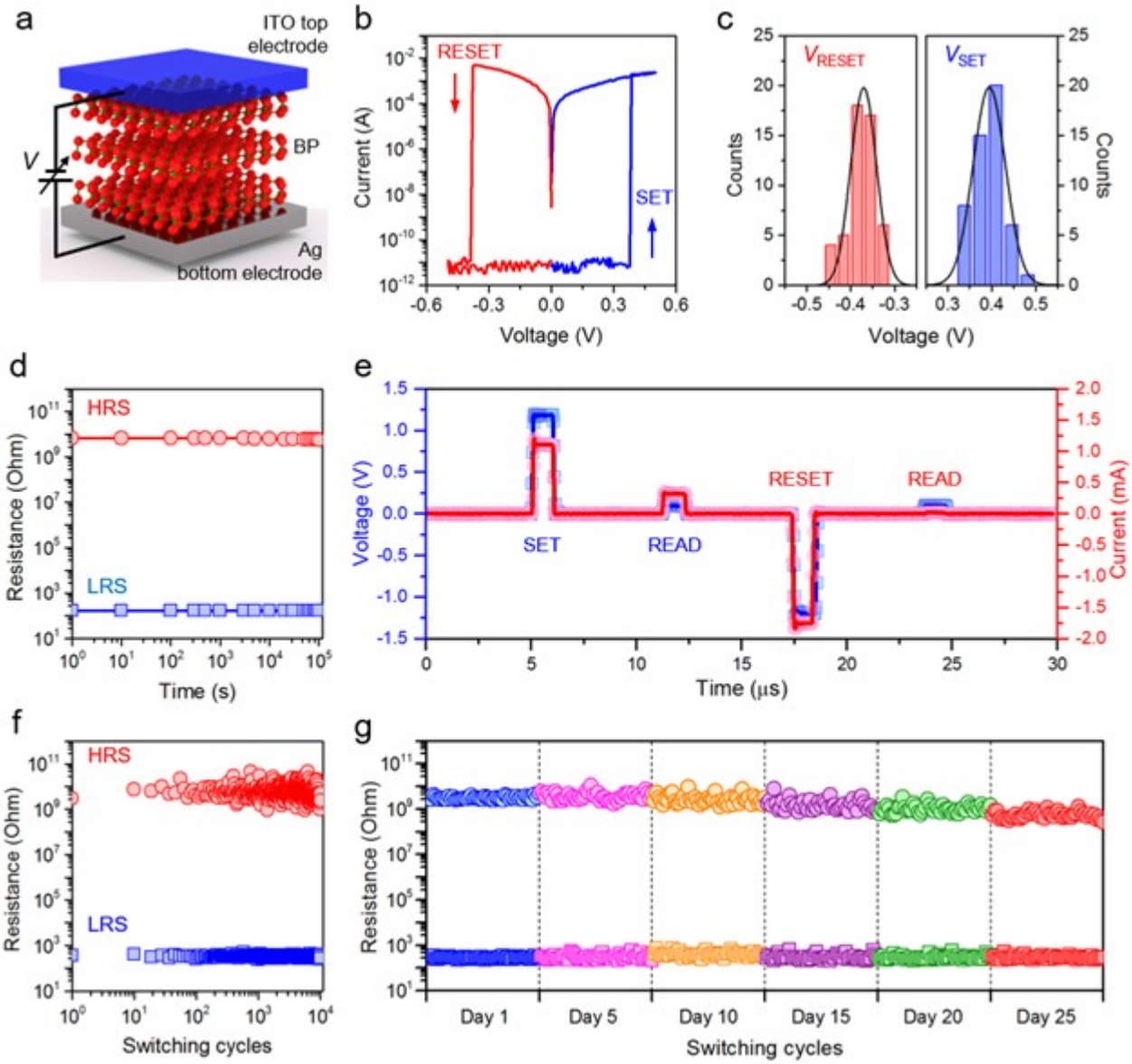

Figure 2. Electrical characterisation of BP resistive memory devices. (a) Schematic illustration of a cross-point BP resistive memory device. (b) *I–V* characteristic sweep of the BP resistive memory devices under ambient conditions. (c) Statistical analysis of V_{SET} and V_{RESET} threshold switching voltages. (d) Time dependent retention characteristics of LRS and HRS for $>10^5$ s. (e) A representative pulsed switching cycle of SET/READ/RESET/READ pulses with the pulse width of

1 μs. A train of SET (1.2 V)/READ (0.1 V) and RESET (-1.2 V)/READ (0.1 V) voltage pulses are applied to the BP resistive memory devices to evaluate cyclic endurance. (f) Pulsed cyclic endurance of a BP resistive memory device for $>10^4$ switching cycles. (g) Stability evalution of BP resistive memory devices assessed by 50 switching cycles after every 5 days.

In their pristine state, the BP resistive memory devices show high resistance and require an irreversible electroforming voltage sweep to initialize the resistive switching behaviour where the magnitude of applied voltage depends on the thickness of BP (see Section S3, Supporting Informtion). The post-electroforming bipolar resistive switching behaviour shows a threshold driven SET/RESET transition (Figure 2b). Such bipolar resistive switching behaviour can be attributed to the localised redox reactions and cation transport across the oxidised BP through conductive filament (as discussed later in manuscript).[6,33] The standby power ($P_{\text{Standby}} = I_{\text{HRS}} \times V_{\text{READ}}$) is estimated to be in the range of <5 fW owing to very low OFF-state currents ($<5\times10^{-12}$ A) observed in our BP resistive memory devices at a READ voltage of 100 mV. Such a low standby power effectively suppresses the leakage current and cell disturbance issues in a memory array.[34] Further, devices fabricated with symmetric top and bottom electrodes of nonreactive metal, such as Au (*i.e.*, Au/BP/Au), do not show any resistive switching. However, by adding a thin layer (~5 nm) of a reactive metal, such as Cr, on the top inteface (*i.e.*, Au/Cr/BP/Au) devices exhibit bipolar resistive switching (see Section S4, Supporting Information). This can be explained by the oxidation of Cr during deposition which adds a metal oxide layer on the surface of BP flake. Under applied bias, oxygen ions from oxidised Cr diffuse into BP, causing interfacial oxidation of BP and induce unstable bipolar resistive switching in Au/Cr/BP/Au devices.[13,16]

Figure 2c shows the statistical distribution of threshold voltages for the onset transition of SET (V_{SET}) and RESET (V_{RESET}) during the cyclic bipolar resistive switching, respectively. The distribution of V_{SET} ranges from 0.33 to 0.48 V with a mean at 0.39 V while V_{RESET} ranges from -0.32 to -0.44 V with a mean of -0.37 V. The stability of resistive states are evaluated under a constant voltage over a long period of time to acquire the retention characteristics. Figure 2d shows the retention of HRS/LRS resistive states for $>10^5$ s, measured at a constant voltage of 100 mV. The ON/OFF ratio is consistently maintained to be $>2\times10^7$ without any deterioration in either of the resistive states. Furthermore, cycle-to-cycle switching performance of the devices is evaluated by applying a train of SET/READ/RESET/READ pulses (Figure 2e). It is worth mentioning that the methods of endurance measurement adopted in several recent papers are debatable, as comprehensively discussed by M. Lanza *et al*.[35,36] As such, following the recommended method of endurance measurements we applied short voltage pulses with a duration of 1 μs to SET (+1.2 V), READ (+0.1 V) and RESET (-1.2 V) the device during each switching cycle (as shown in Figure 2e). Switching speed of our devices are measured to be ~30 ns and ~40 ns for SET and RESET cycles (see Supporting Information, Section 5). Figure 2f shows the electrical endurance of resistive switching for $>10^4$ cycles with high reproduceability. As such, the stable retention characteristics and reproduceable resistive switching show robust non-volatile behaviour of our BP resistive memory devices. It is interesting to note that the resistive switching characterisitcs exhibited by our BP resistive memory devices are superior than several reported cross-point devices based on layered materials, as summarised in **Table 1**.

It is well known that unprotected BP rapidly degrades under the ambient environment[23,37,38] and different strategies have recently been reported to enhance its environmental stability, such as physio-chemical treatment and encapsulation with oxides.[39-42] To evaluate the environmental stability of our cross-point devices, pulsed endurance of our BP memory devices is measured under the ambient uncontrolled conditions. Figure 2g shows the endurance stability with the switching ratio retained at more than 2.1×10^6 for 25 days. The long stability of BP resistive memory devices can be explained by the cross-point structure where the active switching area is encapsulated by top ITO electrode (in the cross-point region) and is not directly exposed to the ambient. Furthermore, diffusion of oxygen ions through layered BP under applied bias and resultant oxide complex stabilizes the ion transport through the device during switching, as discussed below with Raman spectroscopic analysis. As mentioned earlier, BP is prone to oxidation under ambient conditions where humidity and light mainly contribute to its oxidation. As such, we suggest that the environmental stability of our BP devices will further prolong beyond 25 days under vacuum due to the absence of environmental oxygen. Also, the switching performance of our devices should not deteriorate (if not improved) under vacuum because the top ITO electrode serves as an oxygen reservoir for oxygen ion transport required during the resistive switching. It is worth mentioning that Y. Wang *et al.*[13] have thoroughly investigated the effect of phosphorus oxide (P_xO_y) thickness on the resistive switching properties in BP based resistive memory devices. In this study, the P_xO_y was grown under UV exposure and its thickness was controlled by varying UV exposure time. It was suggested that the thickness of P_xO_y does not increase after 10 minutes of UV exposure which indicates depressing oxidation rate of BP after a certain time and exposure. Correlating these findings with our work and addressing

any concerns about P_xO_y thickness variation in our devices, we can confidently assume that oxidation rate of BP under ambient light is relatively slower than exposing under UV which we have comprehensively studied in our another research work.[23] The thickness of P_xO_y will limit itself to <5 nm for <2 hours of ambient exposure during our fabrication processes. As such, all of our BP resistive memory devices have similar thickness of P_xO_y and contribution similar influence in resistive switching characteristics.

During the initial electroforming step, oxygen ions from the top ITO electrode diffuse into the pristine BP layers and result in the formation of localised complex phosphorus oxide (P_xO_y) across the device stack. In the subsequent SET/RESET switching processes, mobile oxygen ions or oxygen vacancies in the localised P_xO_y are driven by the applied electric field inducing resistive switching. As such, the localised oxidation of BP is required during the initial electroforming step to induce resistive switching while the transportation of oxygen ions is facilitated by redox reactions in the localised P_xO_y under SET/RESET voltages. This electric field driven movement of oxygen ions across the device can be identified by a change in Raman peak intensity.[43] Since the transparent top electrode allows to collect Raman spectra from the ITO/BP/Ag cross-point region of the device (Section 2, Supporting Information), we adopt Raman spectroscopic analysis to evaluate the movement of oxygen ions under the influence of switching bias. Raman spectral maps of the cross-point region are collected from a representative device (shown in **Figure 3**a) before and after it is subjected to the resistive switching.

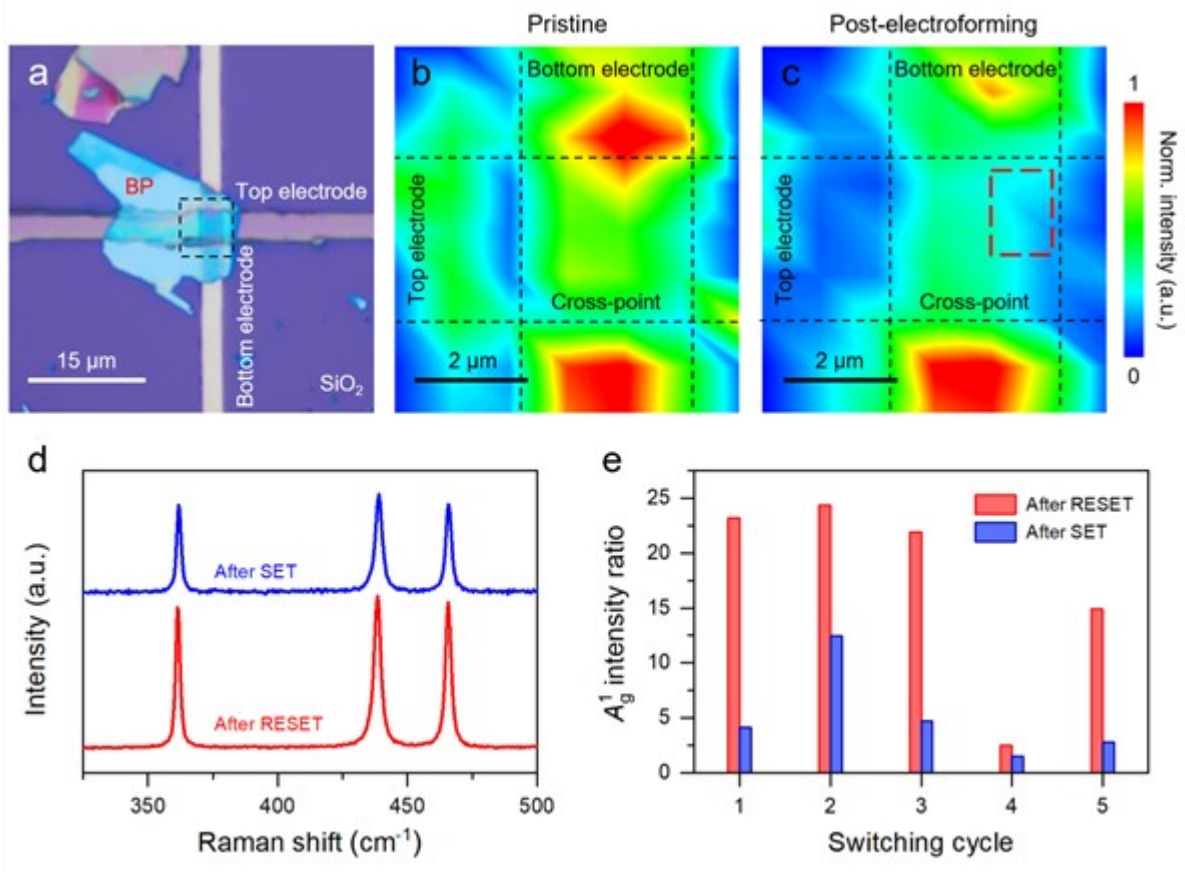

Figure 3. Raman spectroscopic analysis of BP resistive memory devices. (a) Optical microscope photograph of a representative cross-point BP resistive memory device. Raman spectral maps of normalised A^1_g peak intensity collected from a region of interest in (b) pristine (c) after electroforming. *(d) Single-point Raman spectra after a SET and RESET switching cycle.* *(e)* Variation of A^1_g peak intensity with SET and RESET during switching cycles.

Figures 3b and 3c show Raman spectroscopic maps of A^1_g peak intensities on a representative device in its pristine and post electroformed switching states, respectively. The A^1_g peak intensities are normalized to the highest intensity value obtained at a point of interest away from the cross-point region. Comparatively lower normalised intensities are observed in the cross-point region after electroforming (Figure 3c) than the pristine state (Figure 3b). This can be associated with the oxidation of BP under bias conditions.[37,44] Interestingly there is

a variation in the normalised intensity within the cross-point of the device after electroforming where relatively low intensities are recorded from the top right corner of the cross-point (highlighted by an enclosed box in Figure 3c). This suggests that the oxidation of BP and oxygen ion transport in the cross-point are localised which is typical in metal-oxide based resistive memory devices.[45,46] Figure 3d shows single-point Raman spectra for a complete SET/RESET switching cycle, collected from the localised spot in the cross-point region of the switching BP resistive memory device. Comparison of these two single-point spectra reveals that the A^1_g peak intensity after RESET is higher than in LRS *i.e.*, in SET state. To further confirm this trend, single-point Raman spectra are collected for 5 complete SET/RESET switching cycles (see Supporting Information, Section S6, Figure S11). As shown in Figure 3e, the ratio of A^1_g peak intensity is always higher in HRS than in LRS which suggests transport of oxygen ions across the device during resistive switching.[16,43] It is worth mentioning that variation in the ratio of A^1_g peak intensities between different SET/RESET cycles can be associated with the inherent stochastic nature of generation/recombination/migration processes of charge carriers during resistive switching in resistive memory devices.[47,48]

To evaluate the resistive switching mechanism microscopically, cross-sectional high-resolution transmission electron microscope (HR-TEM) and electron energy loss spectroscopic (EELS) analyses are carried out for our BP resistive memory devices. A lamella was cut-out from the cross-point of the representative device (Figure 3a) in HRS after subjected to the resistive switching. Specifically, the area of the cross-point which showed low A^1_g peak intensities in the Raman map (Figure 3c) was included in the lamella. Low magnification TEM micrographs of the lamella reveal that BP switching layer in the

cross-point has both crystalline and amorphous structures (Section S7, Supporting Information). This shows that the region of cross-point which recorded low A^1_g peak intensities has localised oxidation of BP layers to amorphous P_xO_y.

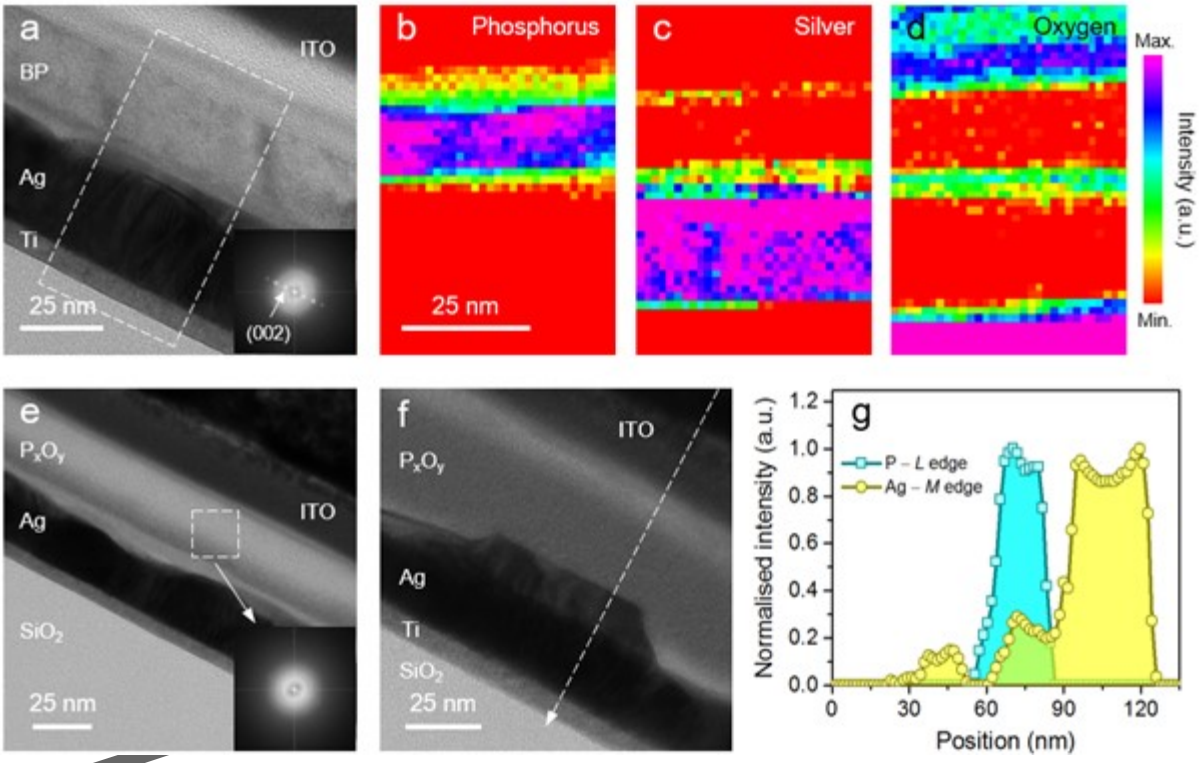

Figure 4. Microscopic characterisation of BP resistive memory devices. (a) Cross-sectional TEM micrograph of pristine section of the representative electroformed ITO/BP/Ag cross-point device. Inset shows FFT diffraction pattern. The EELS area maps of (b) P–*L* edge (c) Ag-*M* edge and (d) O–*K* edge spectra collected from an enclosed region of interest in (a). (e) TEM micrograph of oxidised section of the representative ITO/BP/Ag cross-point device. Inset shows FFT diffraction pattern. (f) HR-TEM micrograph of ruptured Ag protrusion in oxidised BP. (g) The EELS P–*L* edge and Ag–*M* edge profiles along a line scan across the region of interest in (f).

Figure 4a shows HR-TEM micrograph of the non-oxidised section of the cross-point where BP is intact in its crystalline structure, as reflected by the Fast Fourier Transform (FFT) diffraction pattern (inset of Figure 4a). Chemical composition of the crystalline section is

assessed by EELS area maps acquired from a region of interest (highlighted in Figure 4a). The EELS phosphorus (P–*L* edge), silver (Ag–*M* edge) and oxygen (O–*K* edge) area maps are shown in Figure 4b-d, respectively, where maps are generated by taking intensities of the collected spectra (at each pixel) after pre-edge background subtraction. As expected, these EELS area maps reveal that neither BP oxidised nor Ag diffused across the BP layers in this crystalline section of the electroformed cross-point. On the other hand, the HR-TEM micrograph of the oxidised section (Figure 4e) shows amorphous structure of BP layers, confirmed by FFT pattern (inset of Figure 4e). Figure 4f shows a protruded feature from the bottom Ag electrode extending into the P_xO_y layer. The P–*L* edge and Ag–*M* edge spectra collected by EELS line scan (Figure 4g) passing across the P_xO_y layer and protruded feature (highlighted by a dashed line in Figure 4f) reveal that Ag diffused through the P_xO_y layer. This suggests that under an applied bias diffusion of Ag provides a conductive path for charge carriers between top and bottom electrodes in the oxidised section of the device. Further, the decrease of Ag–*M* edge intensities close to the top ITO/P_xO_y interface and relatively high intensities in ITO and P_xO_y layer infer that RESET bias (*i.e.*, negative voltage on bottom Ag electrode) results in the dissolution of Ag conductive path which leads to HRS.[49] Based on the reported literature on electrochemical metallisation memory devices, it can be safely inferred that Ag diffuses from the bottom electrode and migrate across the P_xO_y layer under SET bias to form a conductive bridge resulting in LRS, while RESET bias breaks the conductive path which results in HRS in our BP resistive memory devices.[50-52] To further establish a physical model of resistive switching in our BP resistive memory devices, we model the diffusion of Ag and O atoms through BP multi-layers using density functional theory (DFT) with constrained optimisation (see Experimental). To clarify our

approach, we model the diffusion of the atoms through multi-layer BP while DFT itself will assign the correct charge to the respective atoms. We assume that the bulk BP has a phosphorus vacancy that facilitates diffusion of the Ag and O atom, and we calculate the total energy of the system as a function of the out-of-plane position of the Ag and O atom. This calculation yields the diffusion barrier for the Ag and O atom through stacked van der Waals BP layers as a function of the position of Ag and O atom. As the applied bias (electric field) is perpendicular to the BP layers, it will force O^{2-} and Ag^{+} ions in opposite directions due to their opposite charges. As such, the movement of the Ag and O atoms can be forwards or backwards according to the start and end points.

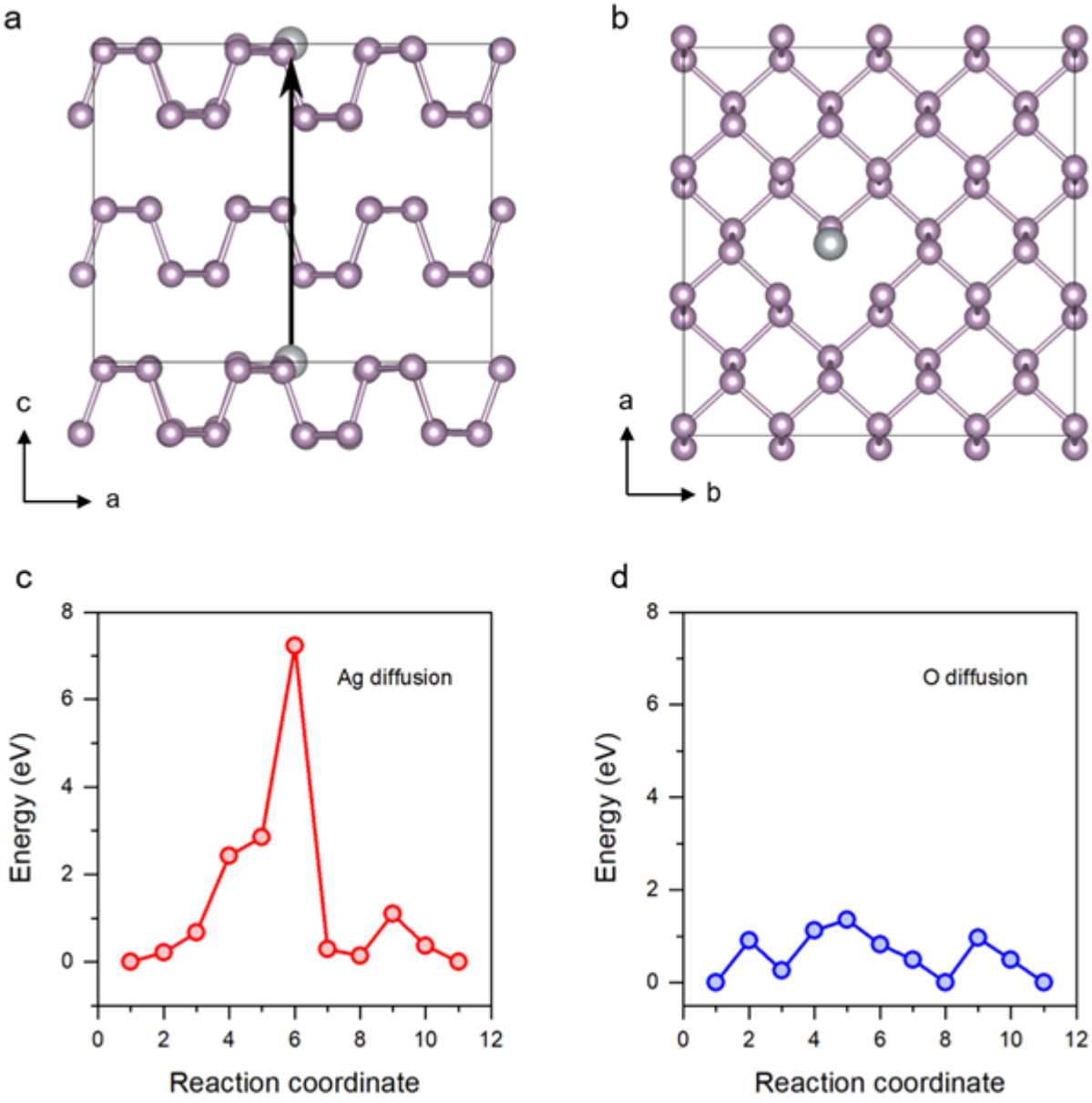

Figure 5. DFT calculations for diffusion barrier energy. Schematic illustration of tri-layer BP crystal structure with (a) side and (b) top view considered as supercell showing a phosphorus vacancy, starting and end point of Ag/O atom (shown as a grey sphere) diffusion pathway indicated by an arrow. The total system energy as a function of the reaction coordinate with the position of (c) Ag atom and (d) O atom.

Figure 5a,b display the structure of a BP supercell containing a phosphorus vacancy as well as the start and end points of the Ag or O atom positions. The change in energy of the system as the Ag and O atom position varies is shown in Figure 5c and 5d, respectively. The barrier for diffusion of an Ag atom is ~7.2 eV, which is significantly larger than for the diffusion of an O atom (~1.4 eV). This clearly shows that the diffusion of O is preferred over that of Ag and an O atom will be more likely to diffuse faster through unoxidized BP when initially an external electric field is applied (*i.e.*, during electroforming process). Moreover, given that the diffusion barriers in Figures 5c,d are for Ag/O through a pristine and a defected layer, the diffusion barrier through bi-layer BP (*i.e.*, a pristine bulk supercell) will have diffusion barrier heights similar to that of the first 5 reaction coordinates in the plots.

Based on the Raman spectroscopy, HR-TEM/EELS analysis and DFT calculations it can be suggested that under the initial applied electric field during electroforming, oxygen diffuses from the top ITO electrode (owing to its comparatively low barrier energy than Ag) resulting in the localised oxidation of BP to amorphous P_xO_y. Diffusion of oxygen ions from partially oxidised top interface and redox reaction under an applied electric field is well reported in oxide base resistive memory devices.[45,53-55] In our case, the top ITO electrode acts as a reservoir for oxygen ions in the ITO/BP stack. Also, the change in Raman A^1_g peak intensity during subsequent SET/RESET is reflected in our Raman spectroscopic analysis which confirms the movement of oxygen ions. Followed by the oxidation of BP, Ag bottom electrode oxidises and under the applied electric field Ag ions diffuse through the localised amorphous P_xO_y, forming a conductive bridge across ITO/P_xO_y/Ag stack. As such, a localised reversible diffusion of oxygen and Ag ions during SET and RESET processes is suggested to form and deplete, respectively, a conductive pathway (*i.e.,* a filament) and

induce stable non-volatile resistive switching behaviour in our BP resistive memory devices. Furthermore, in our devices, BP is ambient exposed and has a thin layer (<5 nm) of P_xO_y on its surface which provides necessary counter electrode reaction for the oxidation of bottom Ag electrode.[56] In several recently reported resistive memory devices, 2D materials are subjected to *ex-situ* oxidation conditions, such as long exposure to ambient, UV and oxygen plasma to grow an oxide layer.[13,14] Based on detailed characterisation of our BP resistive memory devices, we infer that the oxidation of a layered material in a cross-point configuration and under an applied bias lead to a highly reliable resistive switching performance due to high mobility and low barrier energy of oxygen ions in a native oxide.

Conclusions

In summary, we show a 2D material-based memory device that relies on the interplay between the oxygen and silver ion diffusion through the stack. The layered structure of the BP allows for a highly repeatable movement of ions under an applied electric field. Extensive spectroscopic, microscopic and DFT analyses are used to characterize and validate the operation mechanism. The memory device exhibits superior ON/OFF ratios underpinned by extremely low OFF state current, high retention, and endurance. A combination of these is highly desirable for next generation leakage-free memory devices and neuromorphic applications.

Table 1. Comparison of resistive switching characteristics of our BP resistive memory devices with reported 2D materials-based memory devices. Abbreviations — QD: quantum dots, ME: machinal exfoliation, LE: liquid exfoliation, CVD: chemical vapor deposition, NM: not mentioned.

Material	Synthesis method	Thickness (nm)	Top electrodes	Bottom electrode	SET voltage (V)	RESET voltage (V)	Switching ratio	Endurance (cycles)	Retention (s)	Ref
BP	ME	19	ITO	Ag	+0.39	-0.37	$>3.6\times10^7$	1×10^4	1×10^5	This work
BP	ME	15-85	Cu	Au	+0.8	-0.8	1×10^5	NM	1×10^4	[14]
BP	ME	5	Ag	Au	+0.5	-2.0	$\sim2\times10^7$	100	1×10^4	[13]
BP	ME	350	Ag	Pt	+0.5	-1.0	$>1\times10^2$	>100	NM	[57]
BP (thin film)	LE	3000	Al	ITO	+2.0	-2.0	3×10^5	NM	1×10^5	[16]
BP:Polystyrene	LE	40	Al	Al	+3.5	-3.5	6.2×10^2	NM	$>1\times10^3$	[58]
BP-QD:PMMA	LE	4	Al	Al	+2.9	-3.1	2×10^7	100	1×10^4	[15]
SnS	ME	10-40	Ag	Pt	<+0.5	-0.3	10^8	1×10^4	1×10^5	[30]
hBN	CVD	<2	Au	Au	+2.7	-0.866	$>10^6$	1.5×10^3	1×10^4	[29]
hBN	CVD	<2	Ag	Ag	+0.4	--	$>10^{11}$	8×10^4	1×10^3	[29]
hBN	CVD	6	Ti	Au	+4.0	-2.0	1×10^5	1.2×10^3	1×10^7	[12]
hBN	CVD	<5	Graphene	Graphene	~+4.5	-4.5	1×10^2	100	NM	[59]
hBN	CVD	~0.5	Au	Au	~+3.1	-1.0	1×10^7	50	1×10^6	[8]
WS_2	LE	200	Pd	Pt	+0.8	-0.4	1×10^3	NM	$>1\times10^4$	[10]

MoS_2	CVD	>0.7	Au	Au	+2.0	-1.0	$>1\times10^3$	>20	$>1\times10_4$	[19]
MoS_2	CVD	>0.7	Cu	Au	+0.3	-0.3	<10	20	1×10^4	[60]
$MoS_{2-x}O_x$	ME	40	Graphene	Graphene	+2.0	-3.0	~10	$>2\times10^7$	1×10^5	[7]
$MoTe_2$	ME	12	Ti	Au	+2.9	-1.7	1×10^5	NM	1×10^3	[4]
MoO_x	CVD	25	Ti	Pt	+2.5	-2.0	1×10^3	6×10^3	1×10^4	[11]

Materials and Methods

Device fabrication: The BP resistive switching devices were fabricated in cross point configuration. Firstly, an array of Ag (20 nm)/Ti (5 nm) bottom electrodes with average width of ~5 µm were patterned via standard photolithography and deposited by electron beam evaporation (Kurt J Lesker PRO Line PVD 75) on SiO_2 (300 nm)/Si substrates. Then commercially purchased bulk BP crystal (Smart elements, Austria) was used to mechanically exfoliate BP flakes by using the scotch tape method. Mechanically exfoliated micro-flakes were randomly transferred onto the array of bottom electrodes. Samples were then inspected under the optical microscope and atomic force microscope to identify the flakes of interest. After the selection of transferred micro-flakes, top ITO (50 nm) electrodes were patterned in cross-point configuration via standard photolithography (Heidelberg MLA150), lift-off and RF sputtered (Kurt J Lesker PVD 75) in a pure Ar atmosphere at room temperature from a commercial ITO source with In_2O_3:SnO_2 in a 90:10 wt% composition, (Testbourne Ltd.)[45].

Electrical characterization: BP resistive switching measurements were performed using an Agilent 2912A source meter and a Keithley 4200SCS semiconductor characterization system for two-probe measurements.

Transmission electron spectroscopy: The cross-sectional TEM imaging and analysis was carried by lamella cutout from the cross-point by focused ion beam (FIB) using a FEI Scios DualBeam™ system. Cross-sectional micrographs and electron energy loss spectroscopy (EELS) line scans and maps were performed using a JEOL 2100F scanning transmission electron microscope (STEM) with attached Tridium Gatan image filter. The STEM micrographs and EELS spectra were collected using a 1.5 nm beam spot size. The background was fitted using a power law fit and the influence of nearby peaks and plural scattering were reduced by a narrow signal window.

Raman spectroscopy: Spatial Raman peak intensity mapping was conducted on a Horiba LabRAM HR Evolution micro-Raman system equipped with a 9 mW, 532 nm laser, 500 nm lateral resolution and a 50×objective.

Atomic force microscopy and optical characterizations: Thicknesses of the exfoliated BP flakes were measured by topographic scans on a Dimension-Icon AFM in ScanAsyst mode. Optical transmission of the sputtered ITO top electrodes was measured using the CRAIC 20/30 XL UV-Vis micro-spectrophotometer.

DFT calculations: Analytical calculations were performed using DFT as implemented in the Vienna *Ab initio* Simulation Package (VASP).[61] A plane-wave pseudopotential approach was used with the energy cut-off set to 500 eV. A generalised gradient approximation (GGA) in the Perdew-Burke-Ernzerhof (PBE) form was used,[62] with the ion-electron interaction

defined using the projector augmented wave (PAW) method.[63] The effect of van der Waals interactions was accounted by including Grimme's D3 correction.[64] The electronic self-consistent calculation was performed with an energy tolerance of 10^{-5} eV, and the atomic relaxation was performed with a force tolerance of 0.05 eV/Å. The BP layers were modelled using a 3×3×1 supercell with a vacancy in one of the two BP layers. Constrained optimisation calculations were employed to determine the barrier for diffusion along 10 points, spanning the entire *c*-axis of the supercell. The experimental lattice parameters used for BP were with c = 10.5 Å, and therefore the diffusion step of 1.05 Å was considered.

Acknowledgements

This work was performed in part at the Micro Nano Research Facility at RMIT University in the Victorian Node of the Australian National Fabrication Facility (ANFF). Support from the Australian Research Council (LE150100001) is acknowledged.

References

[1] J. J. Yang, D. B. Strukov, D. R. Stewart, *Nat Nanotechnol* **2013**, 8, 13.

[2] D. B. Strukov, G. S. Snider, D. R. Stewart, R. S. Williams, *Nature* **2008**, 453, 80.

[3] E. Linn, R. Rosezin, C. Kügeler, R. Waser, *Nat Mater* **2010**, 9, 403.

[4] F. Zhang, H. Zhang, S. Krylyuk, C. A. Milligan, Y. Zhu, D. Y. Zemlyanov, L. A. Bendersky, B. P. Burton, A. V. Davydov, J. Appenzeller, *Nat Mater* **2019**, 18, 55.

[5] X. Zhu, D. Li, X. Liang, W. D. Lu, *Nat. Mater.* **2018**.

[6] H. Zhao, Z. Dong, H. Tian, D. DiMarzi, M. G. Han, L. Zhang, X. Yan, F. Liu, L. Shen, S. J. Han, S. Cronin, W. Wu, J. Tice, J. Guo, H. Wang, *Adv Mater* **2017**, 29.

[7] M. Wang, S. Cai, C. Pan, C. Wang, X. Lian, Y. Zhuo, K. Xu, T. Cao, X. Pan, B. Wang, S.-J. Liang, J. J. Yang, P. Wang, F. Miao, *Nat Electron* **2018**, 1, 130.

[8] X. Wu, R. Ge, P. A. Chen, H. Chou, Z. Zhang, Y. Zhang, S. Banerjee, M. H. Chiang, J. C. Lee, D. Akinwande, *Adv Mater* **2019**, 31, e1806790.

[9] R. Ge, X. Wu, M. Kim, J. Shi, S. Sonde, L. Tao, Y. Zhang, J. C. Lee, D. Akinwande, *Nano Lett* **2018**, 18, 434.

[10] X. Yan, Q. Zhao, A. P. Chen, J. Zhao, Z. Zhou, J. Wang, H. Wang, L. Zhang, X. Li, Z. Xiao, K. Wang, C. Qin, G. Wang, Y. Pei, H. Li, D. Ren, J. Chen, Q. Liu, *Small* **2019**, e1901423.

[11] F. Rahman, T. Ahmed, S. Walia, E. Mayes, S. Sriram, M. Bhaskaran, S. Balendhran, *Nanoscale* **2018**, 10, 19711.

[12] P. Zhuang, W. Lin, J. Ahn, M. Catalano, H. Chou, A. Roy, M. Quevedo-Lopez, L. Colombo, W. Cai, S. K. Banerjee, *Adv Electron Mater* **2019**, 1900979.

[13] Y. Wang, F. Wu, X. Liu, J. Lin, J.-Y. Chen, W.-W. Wu, J. Wei, Y. Liu, Q. Liu, L. Liao, *Appl Phys Lett* **2019**, 115.

[14] S. Rehman, M. F. Khan, S. Aftab, H. Kim, J. Eom, D.-k. Kim, *J. Mater. Chem. C* **2019**.

[15] S. T. Han, L. Hu, X. Wang, Y. Zhou, Y. J. Zeng, S. Ruan, C. Pan, Z. Peng, *Adv Sci* **2017**, 4, 1600435.

[16] C. Hao, F. Wen, J. Xiang, S. Yuan, B. Yang, L. Li, W. Wang, Z. Zeng, L. Wang, Z. Liu, Y. Tian, *Adv. Func. Mater.* **2016**, 26, 2016.

[17] S. Bhattacharjee, E. Caruso, N. McEvoy, O. C. C, K. O'Neill, L. Ansari, G. S. Duesberg, R. Nagle, K. Cherkaoui, F. Gity, P. K. Hurley, *ACS Appl Mater Interfaces* **2020**, 12, 6022.

[18] K. Wang, L. Li, R. Zhao, J. Zhao, Z. Zhou, J. Wang, H. Wang, B. Tang, C. Lu, J. Lou, J. Chen, X. Yan, *Adv Electron Mater* **2020**, 6.

[19] M. Kim, R. Ge, X. Wu, X. Lan, J. Tice, J. C. Lee, D. Akinwande, *Nat Commun* **2018**, 9, 2524.

[20] C.-X. Zhang, Q. Li, L.-M. Tang, K. Yang, J. Xiao, K.-Q. Chen, H.-X. Deng, *Journal of Materials Chemistry C* **2019**, 7, 6052.

[21] L. Sun, Y. Zhang, G. Han, G. Hwang, J. Jiang, B. Joo, K. Watanabe, T. Taniguchi, Y. M. Kim, W. J. Yu, B. S. Kong, R. Zhao, H. Yang, *Nat Commun* **2019**, 10, 3161.

[22] S. Kuriakose, T. Ahmed, S. Balendhran, V. Bansal, S. Sriram, M. Bhaskaran, S. Walia, *2D Mater.* **2018**, 5, 032001.

[23] T. Ahmed, S. Balendhran, M. N. Karim, E. L. H. Mayes, M. R. Field, R. Ramanathan, M. Singh, V. Bansal, S. Sriram, M. Bhaskaran, S. Walia, *npj 2D Mater. Appl.* **2017**, 1, 1.

[24] H. Tian, Q. Guo, Y. Xie, H. Zhao, C. Li, J. J. Cha, F. Xia, H. Wang, *Adv. Mater.* **2016**, 28, 4991.

[25] T. Ahmed, S. Kuriakose, E. L. H. Mayes, R. Ramanathan, V. Bansal, M. Bhaskaran, S. Sriram, S. Walia, *Small* **2019**, 15, 1900966.

[26] T. Ahmed, S. Kuriakose, S. Abbas, M. J. S. Spencer, M. A. Rahman, M. Tahir, Y. Lu, P. Sonar, V. Bansal, M. Bhaskaran, S. Sriram, S. Walia, *Adv. Func. Mater.* **2019**, 29, 1901991.

[27] Y. Shen, W. Zheng, K. Zhu, Y. Xiao, C. Wen, Y. Liu, X. Jing, M. Lanza, *Adv Mater* **2021**, 33, e2103656.

[28] Y. Li, L. Loh, S. Li, L. Chen, B. Li, M. Bosman, K.-W. Ang, *Nat Electron* **2021**, 4, 348.

[29] S. Chen, M. R. Mahmoodi, Y. Shi, C. Mahata, B. Yuan, X. Liang, C. Wen, F. Hui, D. Akinwande, D. B. Strukov, M. Lanza, *Nat Electron* **2020**, 3, 638.

[30] X. F. Lu, Y. Zhang, N. Wang, S. Luo, K. Peng, L. Wang, H. Chen, W. Gao, X. H. Chen, Y. Bao, G. Liang, K. P. Loh, *Nano Lett* **2021**.

[31] Z. Guo, S. Chen, Z. Wang, Z. Yang, F. Liu, Y. Xu, J. Wang, Y. Yi, H. Zhang, L. Liao, P. K. Chu, X. F. Yu, *Adv. Mater.* **2017**, 29, 1703811.

[32] D. Zhang, Y. C. Wu, M. Yang, X. Liu, C. O. Coileain, M. Abid, M. Abid, J. J. Wang, I. Shvets, H. Xu, B. S. Chun, H. Liu, H. C. Wu, *Sci Rep* **2016**, 6, 30320.

[33] C. Pan, Y. Ji, N. Xiao, F. Hui, K. Tang, Y. Guo, X. Xie, F. M. Puglisi, L. Larcher, E. Miranda, L. Jiang, Y. Shi, I. Valov, P. C. McIntyre, R. Waser, M. Lanza, *Adv Func Mater* **2017**, 27.

[34] X. Feng, Y. Li, L. Wang, S. Chen, Z. G. Yu, W. C. Tan, N. Macadam, G. Hu, L. Huang, L. Chen, X. Gong, D. Chi, T. Hasan, A. V. Y. Thean, Y. W. Zhang, K. W. Ang, *Adv Electron Mater* **2019**, 5.

[35] M. Lanza, H. S. P. Wong, E. Pop, D. Ielmini, D. Strukov, B. C. Regan, L. Larcher, M. A. Villena, J. J. Yang, L. Goux, A. Belmonte, Y. Yang, F. M. Puglisi, J. Kang, B. Magyari-Köpe, E. Yalon, A. Kenyon, M. Buckwell, A. Mehonic, A. Shluger, H. Li, T.-H. Hou, B. Hudec, D. Akinwande, R. Ge, S. Ambrogio, J. B. Roldan, E. Miranda, J. Suñe, K. L. Pey, X. Wu, N. Raghavan, E. Wu, W. D. Lu, G. Navarro, W. Zhang, H. Wu, R. Li, A. Holleitner, U. Wurstbauer, M. C. Lemme, M. Liu, S. Long, Q. Liu, H. Lv, A. Padovani, P. Pavan, I. Valov, X. Jing, T. Han, K. Zhu, S. Chen, F. Hui, Y. Shi, *Adv Electron Mater* **2019**, 5.

[36] M. Lazna, R. Waser, D. Ielmini, J. J. Yang, L. Goux, J. Sune, A. Kenyon, A. Mehonic, S. Spiga, V. Rana, S. Wiefels, *ACS Nano* **2021**.

[37] S. Walia, Y. Sabri, T. Ahmed, M. R. Field, R. Ramanathan, A. Arash, S. K. Bhargava, S. Sriram, M. Bhaskaran, V. Bansal, S. Balendhran, *2D Mater.* **2017**, 4, 015025.

[38] W. Gaoxue, J. S. William, P. Ravindra, P. K. Shashi, *2D Mater.* **2016**, 3, 025011.

[39] S. Kuriakose, T. Ahmed, S. Balendhran, G. E. Collis, V. Bansal, I. Aharonovich, S. Sriram, M. Bhaskaran, S. Walia, *Appl. Mater. Today* **2018**, 12, 244.

[40] S. Walia, S. Balendhran, T. Ahmed, M. Singh, C. El-Badawi, M. D. Brennan, P. Weerathunge, M. N. Karim, F. Rahman, A. Rassell, J. Duckworth, R. Ramanathan, G. E. Collis, C. J. Lobo, M. Toth, J. C. Kotsakidis, B. Weber, M. Fuhrer, J. M. Dominguez-Vera, M. J. S. Spencer, I. Aharonovich, S. Sriram, M. Bhaskaran, V. Bansal, *Adv. Mater.* **2017**, 29, 1700152.

[41] Y. Y. Illarionov, M. Waltl, G. Rzepa, T. Knobloch, J. S. Kim, D. Akinwande, T. Grasser, *npj 2D Mater Appl* **2017**, 1, 23.

[42] P. J. d. Visser, R. Chua, J. O. Island, M. Finkel, A. J. Katan, H. Thierschmann, H. S. J. v. d. Zant, T. M. Klapwijk, *2D Mater* **2016**, 3.

[43] H. Tian, H. Y. Chen, B. Gao, S. Yu, J. Liang, Y. Yang, D. Xie, J. Kang, T. L. Ren, Y. Zhang, H. S. Wong, *Nano Lett* **2013**, 13, 651.

[44] A. Favron, E. Gaufres, F. Fossard, A. L. Phaneuf-L'Heureux, N. Y. Tang, P. L. Levesque, A. Loiseau, R. Leonelli, S. Francoeur, R. Martel, *Nat. Mater.* **2015**, 14, 826.

[45] T. Ahmed, S. Walia, J. Kim, H. Nili, R. Ramanathan, E. L. Mayes, D. W. Lau, O. Kavehei, V. Bansal, M. Bhaskaran, *Nanoscale* **2017**, 9, 14690.

[46] C. F. Chang, J. Y. Chen, C. W. Huang, C. H. Chiu, T. Y. Lin, P. H. Yeh, W. W. Wu, *Small* **2017**, 13.

[47] H. Jiang, D. Belkin, S. E. Savel'ev, S. Lin, Z. Wang, Y. Li, S. Joshi, R. Midya, C. Li, M. Rao, M. Barnell, Q. Wu, J. J. Yang, Q. Xia, *Nat Commun* **2017**, 8, 882.

[48] S. Gaba, P. Sheridan, J. Zhou, S. Choi, W. Lu, *Nanoscale* **2013**, 5, 5872.

[49] Q. Liu, J. Sun, H. Lv, S. Long, K. Yin, N. Wan, Y. Li, L. Sun, M. Liu, *Adv Mater* **2012**, 24, 1844.

[50] Y. Yang, P. Gao, S. Gaba, T. Chang, X. Pan, W. Lu, *Nat Commun* **2012**, 3, 732.

[51] B. K. You, J. M. Kim, D. J. Joe, K. Yang, Y. Shin, Y. S. Jung, K. J. Lee, *ACS Nano* **2016**, 10, 9478.

[52] Z. Wang, S. Joshi, S. E. Savel'ev, H. Jiang, R. Midya, P. Lin, M. Hu, N. Ge, J. P. Strachan, Z. Li, Q. Wu, M. Barnell, G. L. Li, H. L. Xin, R. S. Williams, Q. Xia, J. J. Yang, *Nat. Mater.* **2017**, 16, 101.

[53] T. Ahmed, S. Walia, E. L. Mayes, R. Ramanathan, V. Bansal, M. Bhaskaran, S. Sriram, O. Kavehei, *Sci Rep* **2019**, 9, 1.

[54] T. Ahmed, S. Walia, E. L. Mayes, R. Ramanathan, P. Guagliardo, V. Bansal, M. Bhaskaran, J. J. Yang, S. Sriram, *Appl Mater Today* **2018**, 11, 280.

[55] H. Nili, T. Ahmed, S. Walia, R. Ramanathan, A. E. Kandjani, S. Rubanov, J. Kim, O. Kavehei, V. Bansal, M. Bhaskaran, *Nanotechnology* **2016**, 27, 505210.

[56] S. Tappertzhofen, I. Valov, T. Tsuruoka, T. Hasegawa, R. Waser, M. Aono, *ACS Nano* **2013**, 7, 6396.

[57] X. Yan, X. Wang, B. Xing, Y. Yu, J. Yao, X. Niu, M. Li, J. Sha, Y. Wang, *AIP Advances* **2020**, 10.

[58] Y. L. Hsieh, W. H. Su, C. C. Huang, C. Y. Su, *Nanotechnology* **2019**.

[59] K. Zhu, X. Liang, B. Yuan, M. A. Villena, C. Wen, T. Wang, S. Chen, F. Hui, Y. Shi, M. Lanza, *ACS Appl Mater Interfaces* **2019**, 11, 37999.

[60] R. Xu, H. Jang, M. H. Lee, D. Amanov, Y. Cho, H. Kim, S. Park, H. J. Shin, D. Ham, *Nano Lett.* **2019**, 19, 2411.

[61] G. Kresse, J. Furthmüller, *Phys Rev B* **1996**, 54, 11169.

[62] J. P. Perdew, K. Burke, M. Ernzerhof, *Phys Rev Lett* **1996**, 77, 3865.

[63] P. E. Blöchl, *Phys Rev B* **1994**, 50, 17953.

[64] S. Grimme, J. Antony, S. Ehrlich, H. Krieg, *J Chem Phys* **2010**, 132, 154104.

Use of 2D materials in resistance change memories offer a potential solution to challenges faced by next-generation data storage technologies. Engineering mixed ionic-electronic transport in 2D black phosphorus based vertically stacked memory addresses reliability and standby power consumption issues. Previously invisible localized switching spot is revealed non-destructively with high spatial resolution by a Raman mapping technique.